Biosensors and Bioelectronics 251 (2024) 116117

Contents lists available at ScienceDirect

Biosensors and Bioelectronics

journal homepage: www.elsevier.com/locate/bios

Merging BioActuation and BioCapacitive properties: A 3D bioprinted devices to self-stimulate using self-stored energy

Brenda G. Molina [a,b,c,*], Judith Fuentes [c], Carlos Alemán [a,b,c], Samuel Sánchez [c,d,**]

[a] Departament D'Enginyeria Química, EEBE, Universitat Politècnica de Catalunya, C/ Eduard Maristany 10-14, Ed. I2, 08019, Barcelona, Spain
[b] Barcelona Research Center for Multiscale Science and Engineering, Universitat Politècnica de Catalunya, C/ Eduard Maristany 10-14, Ed. C, 08019, Barcelona, Spain
[c] Institute for Bioengineering of Catalonia (IBEC), The Barcelona Institute of Science and Technology, Baldiri Reixac 10-12, 08028, Barcelona, Spain
[d] Institució Catalana de Recerca I Estudis Avançats (ICREA), Passeig de Lluís Companys 23, 08010, Barcelona, Spain

ARTICLE INFO

Keywords:
C2C12 myoblasts
PEDOT NPs
3D bioprinting
Electroconductive BioInk
BioActuator
BioCapacitor

ABSTRACT

Biofabrication of three-dimensional (3D) cultures through the 3D Bioprinting technique opens new perspectives and applications of cell-laden hydrogels. However, to continue with the progress, new BioInks with specific properties must be carefully designed. In this study, we report the synthesis and 3D Bioprinting of an electroconductive BioInk made of gelatin/fibrinogen hydrogel, C2C12 mouse myoblast and 5% w/w of conductive poly (3,4-ethylenedioxythiophene) nanoparticles (PEDOT NPs). The influence of PEDOT NPs, incorporated in the cell-laden BioInk, not only showed a positive effect in cells viability, differentiation and myotube functionalities, also allowed the printed constructs to behaved as BioCapacitors. Such devices were able to electrochemically store a significant amount of energy (0.5 mF/cm^2), enough to self-stimulate as BioActuator, with typical contractions ranging from 27 to 38 μN, during nearly 50 min. The biofabrication of 3D constructs with the proposed electroconductive BioInk could lead to new devices for tissue engineering, biohybrid robotics or bioelectronics.

1. Introduction

Accuracy of three-dimensional (3D) Computer-Aided Design (CAD) models, coupled with layer-by-layer additive manufacturing, has advanced towards 3D printing, enabling the creation of 3D models with complex shapes and assemblies, efficiently, rapidly and employing a wide variety of materials (Praveena et al., 2022; Ryan et al., 2022; Vu et al., 2022). Nowadays, 3D printing applications can be identified in wearable technologies (Rivera et al., 2022; Zhang et al., 2022; Zhu et al., 2022), fashion (S. S. Wu et al., 2022; Xiao and Kan, 2022), aerospace (Syuhada et al., 2021), food industry (Ma and Zhang, 2022; Outrequin et al., 2023), automotive industry (Ruiz et al., 2022), electronics (Park et al., 2022; Tan et al., 2022), among many other, highlighting its applications in biomedicine (Cho et al., 2021; Pillai et al., 2021; Vu et al., 2022), bioelectronics (Aggas et al., 2020; Asulin et al., 2021; Guo et al., 2019; Yi et al., 2022) and bioengineering, where the process is dubbed as 3D Bioprinting, due to the use of cell-laden inks, bioinks (Kacarevic et al., 2018; Suntornnond et al., 2017).

3D Bioprinting is usually employed to construct 3D cells cultures or living tissues that mimic *in vivo* cell-cell and cell-tissue interactions, resulting in enhanced functions compared to 2D cultures (Demircan Yalcin and Luttge, 2021; Heid and Boccaccini, 2020; Vijayavenkataraman et al., 2018). This technology allows a better understanding of living tissues and the possibility to study novel treatments without the extensive use of animals in biomedical studies. Moreover, biofabrication promotes the utilization of cells functionalities for other applications, for example, the biohybrid valveless pump-bot powered by engineered skeletal muscle reported by Li and coworkers (Li et al., 2019). Muscle rings of C2C12 mouse myoblasts (skeletal muscle cells), were seeded into a hydrogel matrix which, under electrical stimulation, generated contractions employed as a valveless pump, capable of generating unidirectional flow as high as 22.5 μL/min. A similar approach was used by Guix et al. to biofabricate a swimming soft Biohybrid Robots. C2C12 rings were utilized as bioactuators mechanically trained in a serpentine-like skeleton, resulting in improved motion (Guix et al., 2021).

* Corresponding author. Departament d'Enginyeria Química, EEBE, Universitat Politècnica de Catalunya, C/ Eduard Maristany 10-14, Ed. I2, 08019, Barcelona, Spain.
** Corresponding author. Institute for Bioengineering of Catalonia (IBEC), The Barcelona Institute of Science and Technology, Baldiri Reixac 10-12, 08028, Barcelona, Spain.
E-mail addresses: brenda.guadalupe.molina@upc.edu (B.G. Molina), ssanchez@ibecbarcelona.eu (S. Sánchez).

https://doi.org/10.1016/j.bios.2024.116117
Received 20 November 2023; Received in revised form 25 January 2024; Accepted 7 February 2024
Available online 8 February 2024

Currently the main challenge in the progress of 3D bioprinted cultures and its applications, is the design and generation of processable bioinks with specific properties, such as conductivity. Electrical conductivity, which is the ability of electric current to flow through a material (Oliveira et al., 2002), is one of the most desirable properties in medical devices and bioelectronics since the growth and function of cells are affected by electrical signals (Harris, 2021; Wang et al., 2021), nevertheless, the majority of hydrogel-based bioinks are biocompatible but non-conductive. Consequently, researchers are dedicating significant efforts to develop electroconducting hydrogel-based bioinks, merging hydrogels with the electroactive behavior of conducting materials. Recently, Kim and coworkers incorporated hyaluronic acid-modified gold nanoparticles (HA-Au NPs) into a Matrigel/fibronectin hydrogel, improving the electrical conductivity and the actuation of a C2C12 3D cultured muscle (Kim et al., 2022). However, it is widely known that, despite its high conductivity, the main drawback of noble metals is their high-cost (Givan, 2007; Ye et al., 2022) while carbon-based materials can lead to cytotoxicity (Saha et al., 2016; Thakur et al., 2021; Yuan et al., 2019). Contrary, intrinsically conductive polymers (CPs), such as polypyrrole (PPy), polyaniline (PANI), polythiophene (PTh) and, in particular, its derivative poly (3,4-ethylenedioxythiophene) (PEDOT), are an alternative to traditional conducting materials due to its biocompatibility, low-cost, low density, easy processability, and their unique electrochemical and electrical properties (Molina et al., 2020; Ryan et al., 2022). In fact, in 2021, Wang et al. proved that the integration of PEDOT nanoparticles (NPs) into a gelatin methacryloyl (GelMA) hydrogel scaffold, not only enhanced the conductive property, but also promoted myogenic differentiation of C2C12 mouse myoblasts (Wang et al., 2021).

Electroconductive and biocompatible matrices also have applications in bioelectronics, particularly in energy storage devices. These matrices are studied as pseudocapacitive electrode materials in electrochemical capacitors, serving as the primary material in devices capable of storing energy through reversible reduction-oxidation (redox) reactions between the electrolyte and the electrode (Li et al., 2022; Rudge et al., 1994; Wang et al., 2017). When these redox reactions are induced by biological elements (biocatalysts), the devices are referred to as biocapacitors. For example, Sode group reported a biocapacitor based on the enzymatic biocatalyst FAD-dependent glucose dehydrogenase (FADGDH), which transfer electrons from the enzyme to the electrode in presence of glucose, transforming chemical energy into electricity (Hanashi et al., 2009; Kakehi et al., 2007). However, this biocapacitor is limited by the amount of glucose. In contrast, in 2021, Wu et al. utilized an unlimited living biocatalyst for energy conversion and storage. Specifically, Gram-negative *Pseudomonas aeruginosa* (*P. aeruginosa*) bacteria were grown directly on graphene-coated carbon cloth to construct a biocapacitor. In this design, ion exchange is facilitated by mediators excreted from the bacteria and from the C-type cytochrome protein on the cell membrane. The resulting biocapacitor exhibited a capacitance of 1171 F g −1, an energy density of 416 W h kg-1, and an unlimited cycle life with nutritional feeding (X. X. Wu et al., 2022).

Inspired by the current state-of-the-art, this work presents the synthesis of a biocompatible and electroconductive BioInk, conformed by a gelatin/fibrinogen hydrogel matrix, C2C12 mouse myoblast and electroactive PEDOT NPs, to manufacture by 3D Bioprinting living tissues. The response to electrical stimulation has not only enhanced the performance of BioActuators, but has also resulted in a 3D cells culture with the ability to store energy electrochemically, allowing to propose the developed BioInk as material for the fabrication of BioCapacitors for bioelectronics applications, such as self-powered biosensing, biohybrid robots for pulse generation or drug release therapies.

2. Results and discussion

To study the effects and applications of the CP (PEDOT NPs) in the C2C12 mouse myoblast cells laden-hydrogel and vice-versa (*i.e.*, the influence of the skeletal muscle cells on PEDOT NPs), an electroconductive bioink was prepared and 3D bioprinted considering different structures. In brief, electroactive PEDOT NPs were obtained from oxidative polymerization of 3,4-ethylenedioxythiophene (EDOT) using a dodecylbenzenesulfonic acid (DBSA) micelle solution, and initiated with ammonium persulfate (APS). Then, a low concentration of PEDOT NPs (5% w/w) was mixed with a solution containing C2C12 myoblast, gelatin, and fibrinogen (Fig. 1). The resulting solution was 3D bioprinted and cultured for 14 days in conditions that favor cell differentiation and myotube formation. Three different types of structures were prepared (Fig. 1): cylinders, to observe the NPs incorporation; a structure that resembles the infinity symbol, to evaluate cells viability and cells behavior in presence of PEDOT; and square meshes deposited on carbon electrodes to estimate their pseudocapacitive behavior as working electrode in biocapacitors.

2.1. Material characterization

The influence of PEDOT NPs on the chemical structure of the material was evaluated by comparing cylindrical constructs prepared using hydrogels with and without PEDOT NPs. Hereafter, the PEDOT NPs-containing hydrogel has been denoted as Hydrogel-PEDOT while the control hydrogel prepared without PEDOT NPs (*i.e.,* gelatin and fibrinogen alone) is referred to as Hydrogel. The FTIR spectra of neat Hydrogel, Hydrogel-PEDOT and PEDOT NPs are compared in Fig. 2a.

The spectra of Hydrogel and Hydrogel-PEDOT constructs exhibit the characteristic absorption bands of gelatin with the N–H and O–H bands at 3285 cm-1, the peaks of amide I (C═O stretching) at 1629 cm-1, amide II (C–N–C═O symmetry stretching and N–H in-plane bending) at 1536 cm-1, the symmetrical stretching of the –COOH groups at 1447 cm-1, and amide III (C–N stretching) at 1240 cm-1 (Abdollahi Baghban et al., 2021; de Souza et al., 2023; Rohde et al., 2022). Besides, the spectrum of PEDOT NPs showed the characteristic bands of PEDOT with the fundamental vibrations of the thiophene ring at 1636 and 1563 cm-1, the vibrational bands associated to the C–O–C stretching from the ethylenedioxy group at 1204 and 1046 cm-1, and the C–S stretching at 691 cm-1 (Molina et al., 2018; Puiggalí-Jou et al., 2017). Unfortunately, such bands were not detected in the spectrum of Hydrogel-PEDOT construct, which was clearly dominated by the gelatin absorption bands due to low concentration of PEDOT NPs (5% w/w). Therefore, chemical characterization of the constructs was completed using Raman spectroscopy (Fig. 2b).

Contrary to FTIR spectroscopy, Raman spectrum of Hydrogel-PEDOT was dominated by the PEDOT NPs signal, with peaks at: 1425 and 1430 cm^{-1} respectively, associated with the C═C symmetrical stretching, 1364 cm^{-1} for C_β–C_β stretching vibrations, 1262 cm^{-1} due to C_α–C_α inter-ring stretching, 988 cm^{-1} related with O–C–C–O ring deformation and at 860 cm^{-1} for the asymmetric C–S–C deformation, all these fingerprints were also observed in PEDOT NPs spectrum (Kong et al., 2022; Molina et al., 2021). On the other hand, the absence of NPs in the Hydrogel constructs, revealed the main Raman signatures of the gelatin with C═N stretching vibration at 1669 cm^{-1}, CH stretching and scissoring of methyl (CH3) and methylene (CH2) at 1452 cm^{-1}, CH wagging at 1341 cm^{-1} and amide III (C–N stretching) at 1207 cm^{-1} (Abdollahi Baghban et al., 2021; Rohde et al., 2022).

The physical appearances of the constructs can be observed in Fig. 3a (left), where the whitish Hydrogel turns into a homogeneous dark blue color, as result of the incorporation of PEDOT NPs. Meanwhile, Fig. 3a (center) shows a representative micrographs of PEDOT NPs with a typical coral-like morphology and an effective diameter of 540 ± 279 nm (Fig. 3a right) (Molina et al., 2018; Puiggalí-Jou et al., 2017).

Hydrogel and Hydrogel-PEDOT constructs present a characteristic gel porous morphology (Freeman et al., 2019; Rafienia et al., 2008; Shengjie et al., 2009; Zheng et al., 2021), displayed in Fig. 3b and c (left), respectively. However, higher magnitudes focused on the pores

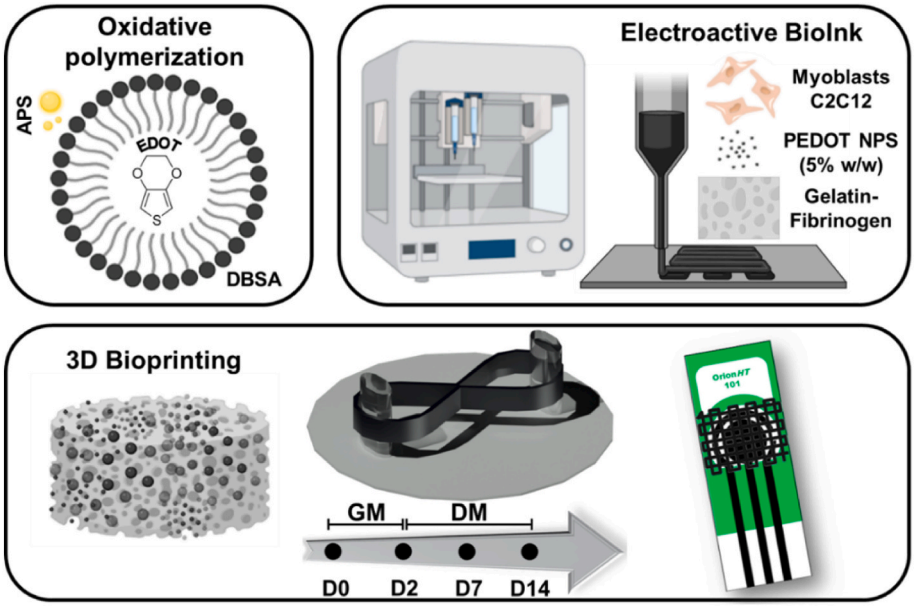

Fig. 1. Schematic representation of the electroconductive bioink synthesis (top) and the 3D printed constructs (bottom), from left to right: cylindrical structure, infinity-like structure, and square mesh onto a carbon electrode (Orion*HT* 101). Partially created with BioRender.com.

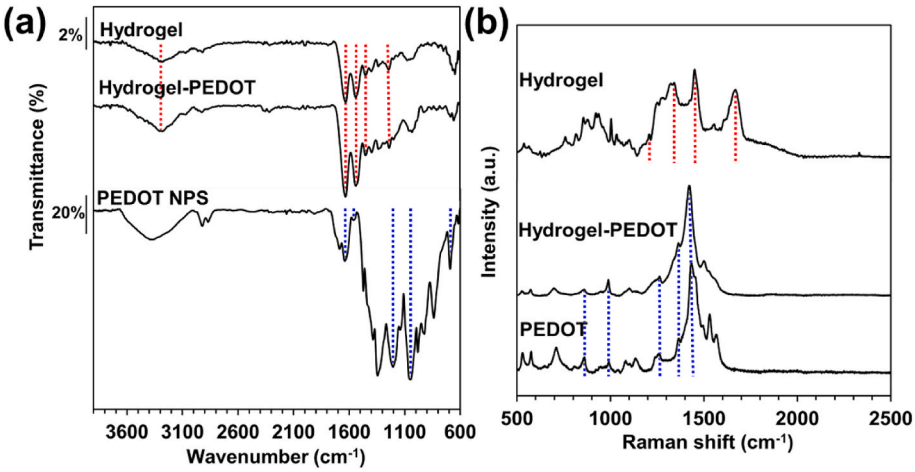

Fig. 2. (a) FTIR and (b) Raman spectra for the neat Hydrogel, Hydrogel-PEDOT and PEDOT NPs.

border line (Fig. 3b and c center), revealed that PEDOT NPs transformed the smooth Hydrogel surface into a rough one with coral-like agglomerates. Nevertheless, the pore size average of both materials was similar, 133 ± 88 μm for the Hydrogel and 104 ± 54 μm for the electroactive Hydrogel-PEDOT (Fig. 3b and c right). The relevance of the pore size lies in its relationship with the material ability to absorb liquid medium, that in 3D Bioprinting cultures is fundamental to provide nutrients for growing cells and support cell migration. In concordance with the pore size, the swelling ratio (SR) obtained from Hydrogel and Hydrogel-PEDOT was alike, with 1027 ± 144 % and 1086 ± 51 %, respectively, demonstrating that the incorporation of the CP has no negative effect in one of the principal properties for a 3D Bioprinted constructs.

2.2. 3D bioprinted constructs characterization

Previous results confirmed the successful incorporation of PEDOT NPs into gelatin-based hydrogels, therefore, the next step was the preparation of two bioinks to 3D bioprint and evaluate C2C12 cells viability, contraction force and self-stimulation in presence of PEDOT NPs. An infinity-like design was carefully selected and bioprinted between two polydimethylsiloxane (PDMS) posts to favor cells alignment, as shown in Fig. S1a (left). The constructs were incubated for 2 days in growth medium (GM) and 12 days in differentiation medium (DM) to promote cells differentiation and myotube formation, which led to the compaction of the cell-laden hydrogels, as shown in Fig. S1a (right).

2.2.1. Cell viability

The biocompatibility of constructs obtained from the two prepared bioinks, hereafter referred to as C2C12 Hydrogel and C2C12 Hydrogel-PEDOT, was assessed by monitoring the metabolic activity through a non-invasive PrestoBlue™ assay for several incubation days. The resulting data are presented in Fig. 4a. The normalized absorbance increased steadily during the initial days of incubation, attributed to the proliferation of C2C12 cells. By the tenth day of measurement, exponential growth reached a plateau, indicating the differentiation of C2C12 myoblasts into myotube cells or cellular senescence, stabilizing the metabolic activity. This process occurred faster for C2C12 Hydrogel-PEDOT (day 10) than for C2C12 Hydrogel (day 12), suggesting that PEDOT NPs could enhance cell proliferation. No significant decrease in

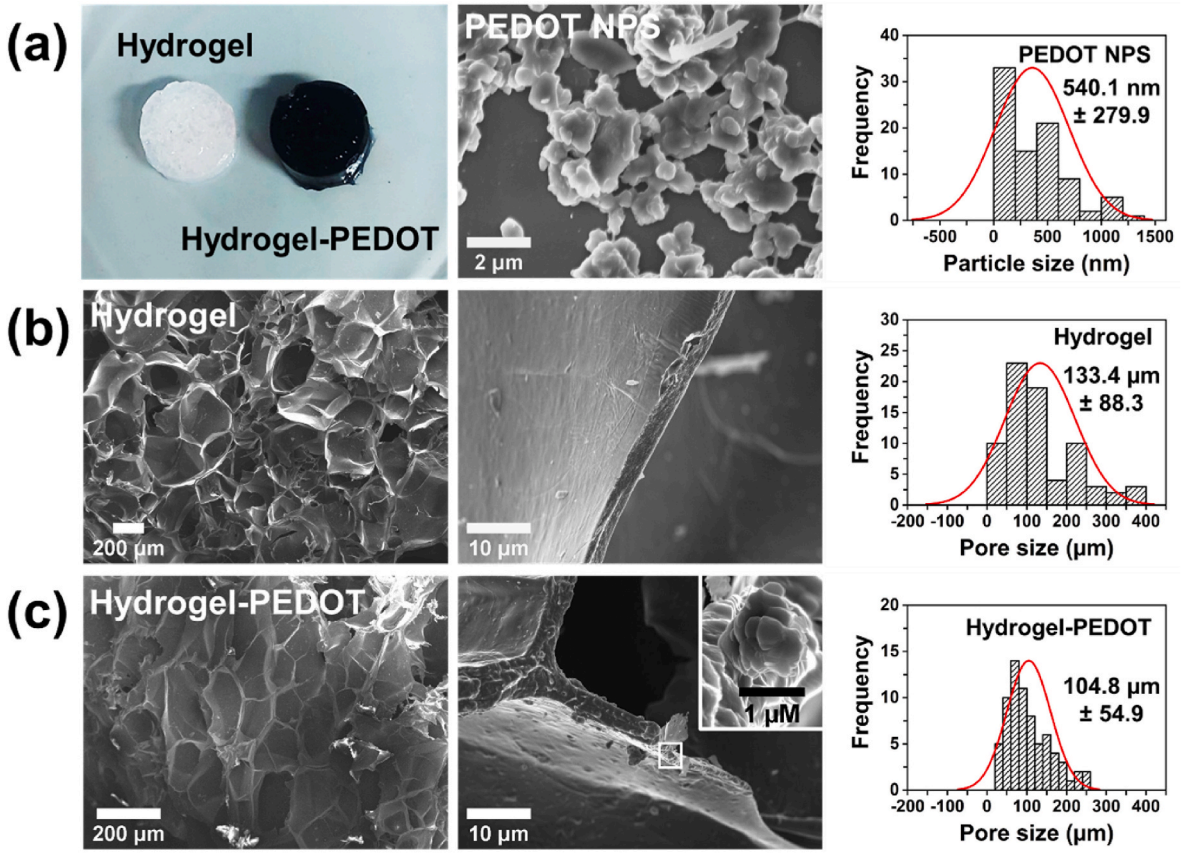

Fig. 3. From left to right (a) representative photograph of Hydrogel and Hydrogel-PEDOT cylinders, SEM micrographs of PEDOT NPs and particles size distribution histogram. Low and high magnifications of SEM micrographs, and pore size distribution histogram for (b) Hydrogel and (c) Hydrogel-PEDOT constructs.

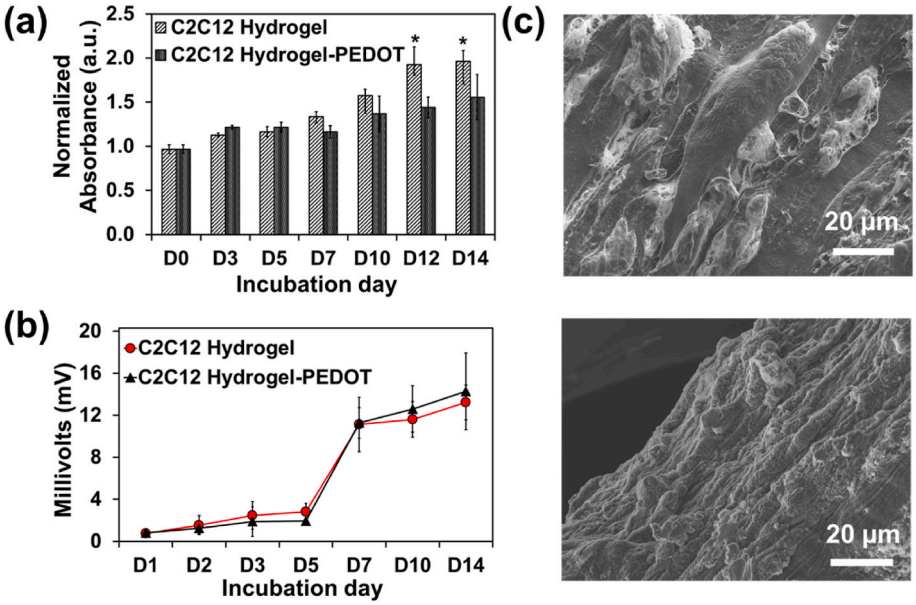

Fig. 4. (a) Cells viability and (b) voltage across 3D bioprinted constructs at different incubation days, from day 0 (D0) until day 14 (D14) ($n = 3$). Asterisks indicates significant difference ($p < 0.05$; following a two-way ANOVA with Tukey's post-test compared with controls). (c) SEM micrographs of the construct surface after 14 incubation days: top C2C12 Hydrogel; and bottom C2C12 Hydrogel-PEDOT.

absorbance was recorded, demonstrating that neither the bioinks, the 3D bioprinting process, nor subsequent crosslinking were toxic for the cells. Hence, the viability of cell-laden constructs was evident even in the presence of PEDOT NPs.

Viability studies were completed adapting the transepithelial/endothelial voltage assay (TEV) to assess the effect of conductive PEDOT NPs in the cell membrane potential generated by the C2C12 cells at different incubations days. Previous studies reported that the potential

of living cell membranes is similar to that in the surrounding extracellular medium and, since the membrane of a dead cell becomes perforated, cellular death obstructs the traffic of ions, hence, the potential of the extracellular medium decreases (Frömter and Diamond, 1972; Gerasimenko et al., 2020; Rühl et al., 2021). Fig. 4b exhibits the tendency of the voltage recorded across the constructs. As expected, the behavior was similar to the results obtained from the PrestoBlue™ assay, the voltage in the constructs increased constantly and reach a plateau at day 10. These results confirm cells proliferation in the constructs, no detrimental effect was associated to the incorporation of PEDOT NPs.

Qualitative SEM micrographs of C2C12 Hydrogel and C2C12 Hydrogel-PEDOT surfaces after 14 incubation days were obtained as shown in Fig. 4c. Micrographs revealed C2C12 cells aligned and elongated, suggesting myotube formation and, therefore, maturation of the bioprinted tissue. Cells alignment was promoted by the 3D bioprinting extrusion-based process and by the tension force generated through the two PDMS posts when the constructs shrink or contract, as perceived in Fig. S1a. Meanwhile, myotube formation was promoted by the incubations conditions, specifically, by the differentiation media (DM). Previous investigations suggest that similar tissues under this conditions could lead to sarcomere structures (Mestre et al., 2021), which are responsible for the contraction and relaxation of muscle fibers in response to neural stimuli (Ahmed et al., 2022; Labazanova et al., 2021). Hence, force contraction measurements were performed.

2.2.2. Force contraction and self-stimulation

The functionality of 3D bioprinted constructs (*i.e.,* differentiation and myotube formation of cells laden into C2C12 Hydrogel and C2C12 Hydrogel-PEDOT) was evaluated by contraction studies, mimicking neural stimuli with electrical stimulation (EST) at day 14 of incubation. The biofabricated constructs were exposed to electric frequencies from 0 to 10, 15 or 20 V and, at the same time, the response of the constructs was investigated by the displacement of the PDMS post (x). A representative scheme is shown Fig. 5a, while normalized displacement recorded as response of C2C12 Hydrogel and C2C12 Hydrogel-PEDOT under EST with a maximum voltage of 10, 15 or 20 V are compared in Fig. 5b–d. In all cases, posts movements evidenced that EST induced contraction in the 3D bioprinted constructs, confirming the tissues response, functionality and a behavior related with bioactuators or artificial muscles. Moreover, the performance of the bioactuators, here denoted as C2C12 Hydrogel and C2C12 Hydrogel-PEDOT, under EST followed the applied frequencies (1 Hz) in a synchronous manner, producing twitch contractions. The homogenous electrical response in the constructs body are illustrated in the Supplementary Videos 1 and 2 for C2C12 Hydrogel and C2C12 Hydrogel-PEDOT, respectively. Finally, comparison of the post displacement distance in Fig. 5b–d reveals the positive effect of electroactive PEDOT NPs. Thus, C2C12 Hydrogel-PEDOT contraction response was improved among 20% and 50% with respect the C2C12 Hydrogel at different voltages conditions that, as expected, is proportional to displacement distance.

Supplementary video related to this article can be found at https://doi.org/10.1016/j.bios.2024.116117

The strength of the contractions was calculated converting posts displacement distance into force units (N) employing the classical Euler–Bernoulli beam bending theory (Eq (1)):

$$\mathrm{P}\,(N) = \frac{3EI_z x}{a^3} \qquad \text{(Eq. 1)}$$

where P is the applied force, E the Young's modulus of PDMS (206 KPa), I_z the second moment of area of the post around the z-axis, a the height at which the tissue is placed (calculated from z-Stack images), and x the displacement of the post at that height.

Fig. 5e show the calculated force for each bioactuator at different conditions of EST. Consistently, forces contractions calculated for C2C12 Hydrogel-PEDOT were superior to bare C2C12 Hydrogel, due to PEDOT conductive nature. The electronic and ionic conductivity of PEDOT NPs

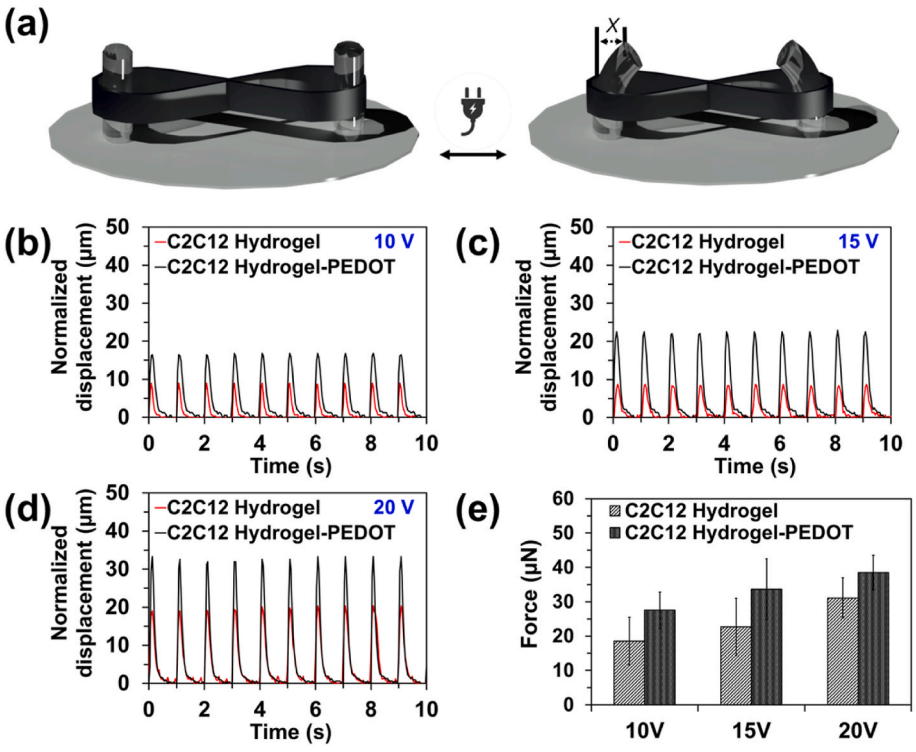

Fig. 5. (a) Representative scheme of PDMS posts displacement as result of constructs contraction under electrical stimulation. Normalized posts displacement recorded when C2C12 Hydrogel and C2C12 Hydrogel-PEDOT constructs were stimulated with electrical frequencies of 1 Hz, an amplitude of 2 ms, and voltage from 0 V to (b) 10 V, (c) 15 V or (d) 20 V. (e) Force measurements of C2C12 Hydrogel and C2C12 Hydrogel-PEDOT under electrical stimulation ($n = 3$). Asterisks indicates significant difference ($p < 0.05$ with Tukey's post-test).

allowed: *i)* higher levels of charge injection across the bioactuator, *ii)* decrease the impedance at the interface between the carbon electrode and the tissue, and *iii)* increase the charge storage capacity of the construct (Ganji et al., 2017; Sordini et al., 2021; Wang et al., 2021).

During differentiation time (12 days), spontaneous contractions were not observed. Nevertheless, after force contraction experiments, C2C12 Hydrogel-PEDOT samples exhibited unprompted activity, therefore, self-stimulations tests were conducted. For this purpose, 3D bioprinted constructs were exposed to EST, from 0 to 20 V during 5 min, recording the last 10 s and, the bioactuator's response with no EST every 10 min for 1 h. Results are presented in Fig. 6 and Supplementary Videos 3 and 4. The contractions during the initial 10 s, correspond to constructs performance under EST, and agree with previous results of higher contraction force in presence of PEDOT NPs. However, once EST was halted, C2C12 Hydrogel construct displayed multiples and uncontrolled contractions during approximately 2.5 s, which decreased gradually its intensity until no signal was recorded in almost 10 s (Fig. 6a). Contrary, after EST, C2C12 Hydrogel-PEDOT continued showing activity (Fig. 6b), where well-defined twitch contractions were merged into faster force contractions, a process referred to as summation, that continued for more than 50 min. This behavior could be associated to redox reactions from extracellular proteins (Manabe et al., 2014), Adenosine triphosphate (ATP) (Araya et al., 2004; Bustamante et al., 2014) or Ca^{2+} (Cho et al., 2017; Germinario et al., 2008; Lamport and Várnai, 2013) released by C2C12 cells, which converts them in living biocatalyst. The ion exchange in presence of electroactive PEDOT NPs transform the chemical energy into electricity, leading to the bioactuator C2C12 Hydrogel-PEDOT performs as biocapacitor, and self-stimulate for a long term.

Supplementary video related to this article can be found at https://doi.org/10.1016/j.bios.2024.116117

2.2.3. Electrochemical characterization and capacitor behavior

In order to understand the storage charge capacity of the bioactuator C2C12 Hydrogel-PEDOT and, therefore, its performance as biocapacitor, 3D printed square meshes (Fig. S1b) were utilized as working electrode in electrochemical assays. For the sake of completeness, measurements were also conducted using constructs prepared from Hydrogel and Hydrogel-PEDOT Inks as controls, along with the bioink C2C12 Hydrogel.

The ability of the constructs to exchange charge, meaning electrochemical activity or electroactivity, was determined by cyclic voltammetry (CV) recorded on incubation days 0 and 14. As observed in Figure S2a, the four samples exhibited very similar voltammograms, both in terms of current intensity (*j*) values and shape of the voltammograms. However, when the electrochemical stability was evaluated (Eq S2), summing the anodic and cathodic areas of the voltammograms from 0 to 100 redox cycles (Fig. 7a), the constructs without PEDOT NPs, Hydrogel and C2C12 Hydrogel, presented a loss of electroactivity of 37 ± 17 and 36 ± 13 %, with only 10 redox cycles, while, Hydrogel-PEDOT and C2C12 Hydrogel-PEDOT constructs after 100 redox cycles only lost 9 ± 1 and 7 ± 1 % of electroactivity, respectively. These results indicate that C2C12 cells do not significantly affect the electroactivity of the systems. Furthermore, results obtained for Hydrogel and C2C12-Hydrogel show that the ion exchange from the electrolyte medium and the constructs during reduction and oxidation processes collapses the hydrogel structure, decreasing the electrostability. However, in presence of PEDOT NPs, ion exchange occurs directly on the conductive polymer (CP), preventing structural failure and, consequently,

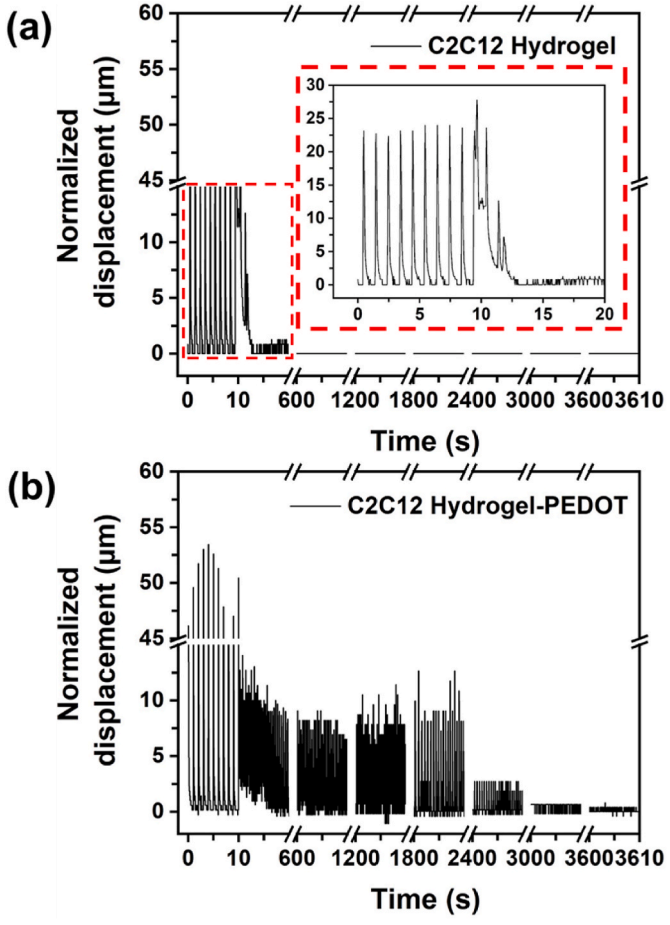

Fig. 6. Normalized post displacement recorded from self-stimulation tests, acquired after electrical stimulation of 1 Hz from 0 to 20 V and 2 ms of amplitude, for (a) C2C12 Hydrogel (insert, zoom of initial 20 s) and (b) C2C12 Hydrogel-PEDOT.

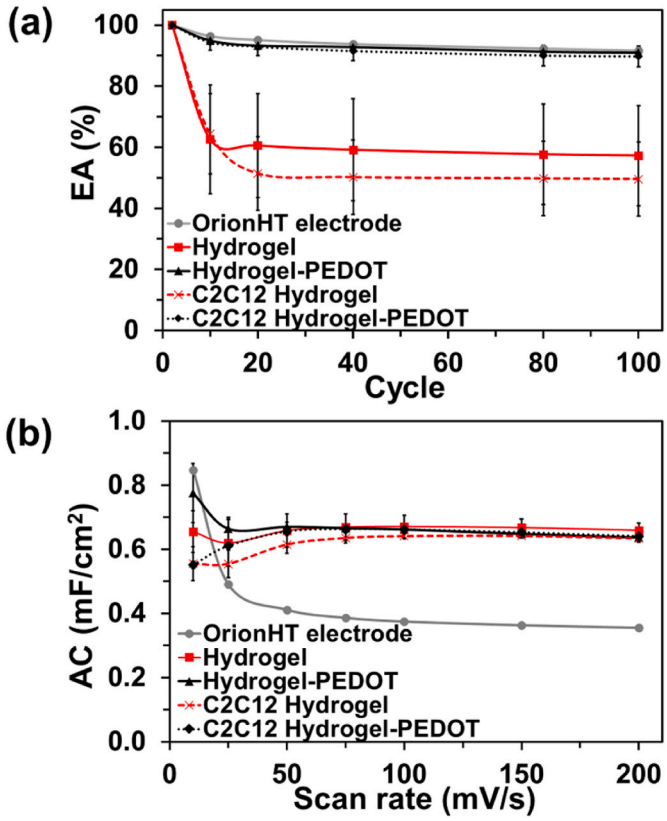

Fig. 7. (a) Evolution of the electrochemical activity (EA) with the number of redox cycles and (b) areal specific capacitance (AC) determined from cyclic voltammetry (CV) at different scan rates (n = 3).

extending the electrostability.

Regarding the capacitance, CV was also employed to obtain the areal capacitance (AC) of the studied samples. For that, voltammograms were recorded at day of incubation 14 with different scan rates (10, 25, 50, 75, 100, 150 and 200 mV s^{-1}). Results are displayed in Figure S2b and summarized in Fig. 7b. All the voltammograms exhibit an ideal symmetric rectangular shape, which indicates good capacitive performance, low contact resistance and notable reversibility (Pérez-Madrigal et al., 2017; Ruano et al., 2021). Meanwhile, the average AC obtained applying Eq S3 proved the capacitance performance of the constructs, especially when compared with the low capacitance of the bare carbon OrionHT electrode (Fig. 7b).

Galvanostatic charge/discharge (GCD) tests were used to assess the energy storage of the four constructs charged at different currents density 0.02, 0.04 or 0.08 mA/cm^2. The curve of voltage *vs.* time from GCD measurements, which were performed at 0.6 V window, are displayed in Figure S3. The graphs show the typical triangle-like shape associated with the charge and discharge times, revealing that the constructs with PEDOT NPs charged faster, independently of the current density applied. This observation confirms that the CP improve charge injection across the constructs and the interfacial impedance between the electrolytic medium and working electrode. Average AC obtained from GCD and Eq S4 are presented in Fig. 8a and b.

The cyclability or capacitance stability was evaluated submitting the constructs to 300 consecutive GCD cycles, from 0 to 0.6 V at a current density of 0.04 mA/cm^2. Figure S4 shows all the cycles, while the first (solid line) and 300th cycle (dotted line) are explicitly displayed in Fig. 8c and d. As mentioned in previous discussions, the constant ion exchange in the Hydrogel samples collapse the internal structure, which was evidenced with the drastic change of GCD curves before and after 300 consecutive cycles. This effect also promotes the AC increase since after some cycles the internal collapse stops and the structure self-stabilizes (Ruano et al., 2021). This feature explains the enhancement of the AC, which is 101% ± 14% and 41% ± 17% for Hydrogel and Hydrogel-PEDOT, respectively (Fig. 8e). The attenuated effect in the latter has been associated to the benefits of the PEDOT NPs. Contrary, AC of cell-laden constructs after 300 consecutive GCD cycles decreased 15% ± 0.3% and 28% ± 0.7% for C2C12 Hydrogel and C2C12 Hydrogel-PEDOT, respectively (Fig. 8e). C2C12 Myotubes formed into the constructs act as reinforce fibers for the matrix material, reducing the internal collapse while at the same time allow the ion exchange. Accordingly, the AC grows from 0.4 ± 0.1 mF/cm^2 for C2C12 Hydrogel to 0.5 ± 0.0 mF/cm^2 for C2C12 Hydrogel-PEDOT.

Finally, leakage-current and self-discharging responses were observed after charging the studied constructs to 0.6 V at 0.005 mA. Fig. 9a demonstrates that, as a constant voltage is maintained, the current gradually decreases in all four systems. However, the current stabilizes at higher values for Hydrogel and Hydrogel-PEDOT constructs, indicating a better stability than C2C12 Hydrogel and C2C12 Hydrogel-PEDOT, where the applied voltage affected negatively the cell-laden. On the other hand, Fig. 9b illustrates the voltage drop of charged systems. Hydrogel and Hydrogel-PEDOT exhibit minimal resistance to be self-discharged in comparison to C2C12 Hydrogel and C2C12 Hydrogel-PEDOT. The loss of charge exhibited in the former was of 79 and 77 %, respectively, after only 100 s, while during the same period C2C12 Hydrogel and C2C12 Hydrogel-PEDOT were discharged 55% and 38%, respectively. These results reflect that the combination of redox reactions from C2C12 cells and electroactive PEDOT NPs promotes a

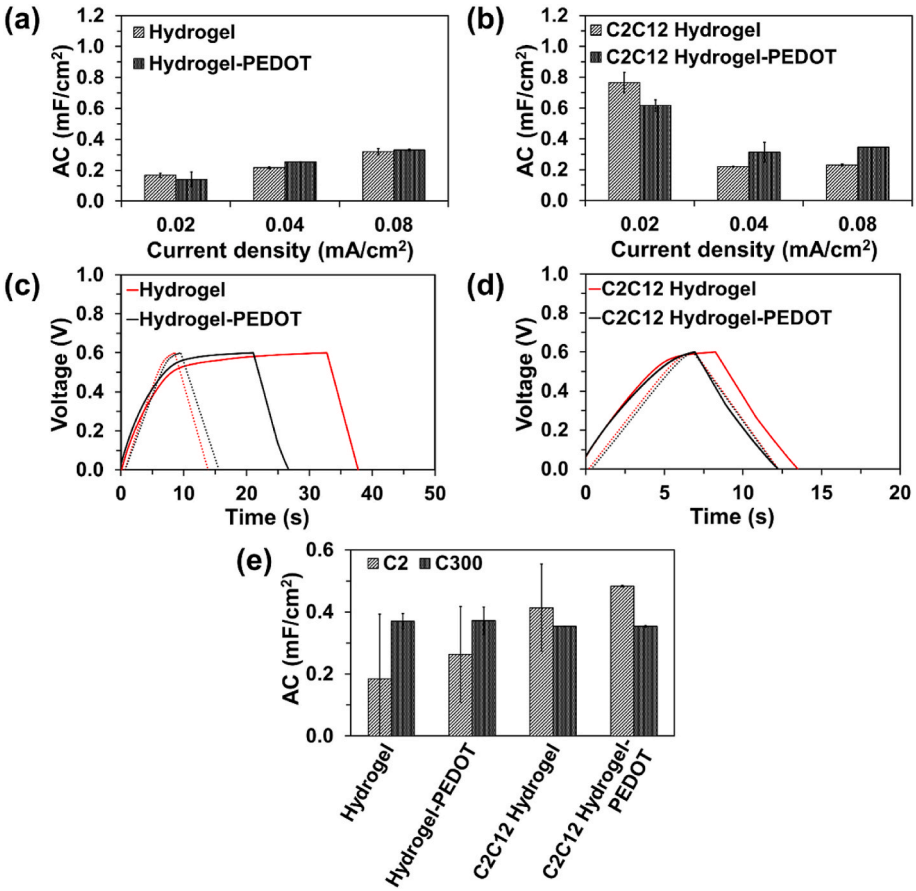

Fig. 8. (a–b) Areal specific capacitance (AC) determined from galvanostatic charge/discharge (GCD) assays at different currents, 0.02, 0.04 or 0.08 mA/cm^2 ($n = 3$). (c–d) Cyclability test determined from the 1st and 300th GCD cycle, recorded from 0 to 0.6 V at a current density of 0.04 mA/cm^2 for (c) Hydrogel, Hydrogel-PEDOT, (d) C2C12 Hydrogel and C2C12 Hydrogel-PEDOT. (e) AC determined from GCD before and after with 300 consecutive GCD cycles ($n = 3$).

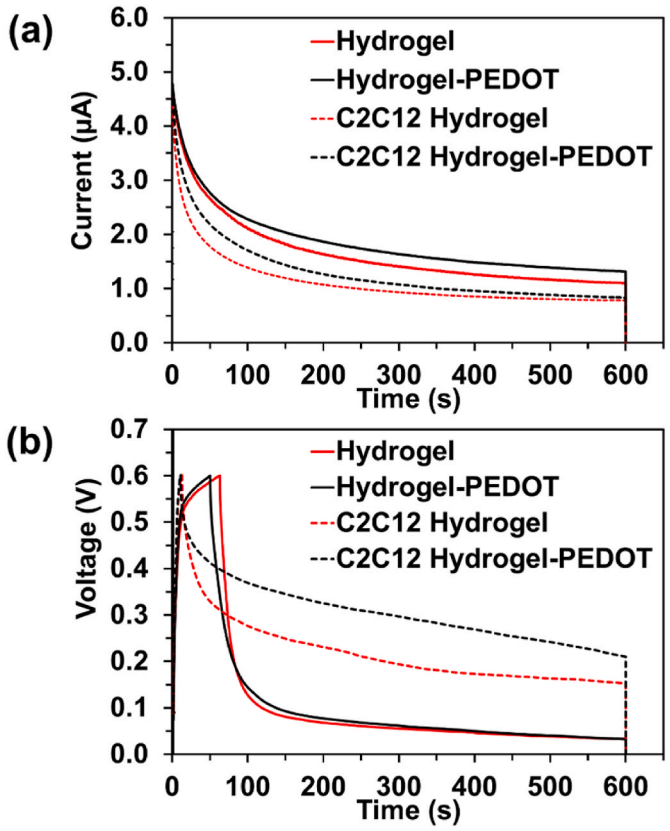

Fig. 9. (a) Leakage current and (b) voltage drop curves after charging to 0.6 V at 0.005 mA.

higher capacity to store energy electrochemically, suggesting a promising application of the C2C12 Hydrogel-PEDOT constructs as biocapacitors.

3. Conclusions

Electroactive PEDOT NPs prepared by oxidative polymerization, have been successfully incorporated into a C2C12 cell-laden hydrogel solution based in gelatin and fibrinogen. The resulting electroconductive BioInk has been used to create three different constructs (cylinder, infinity-like structure, and a square mesh printed directly onto the surface of a carbon electrode) using extrusion-based 3D printing technique. The homogenous and correct incorporation of PEDOT NPs was confirmed through the cylinder constructs, while the infinity-like constructs allowed to confirm the biocompatibility of PEDOT NPs and validate the use of the electroconductive BioInk for manufacturing an improved BioActuator. The latter exhibited stronger contractions forces due to the enhanced response to electrical stimulation. Additionally, the electroconductive BioInk was also employed to 3D Bioprint a Bio-Capacitor with amplified capacity to store energy electrochemically (0.5 mF/cm2), sufficient to self-stimulate the BioActuator for almost 50 min. In summary, the remarkable properties and versatility of constructs obtained though the 3D Bioprinting with the proposed electroconductive BioInk open new perspectives and applications in tissue engineering, biohybrid robotics or bioelectronics.

CRediT authorship contribution statement

Brenda G. Molina: Writing – review & editing, Writing – original draft, Methodology, Investigation, Formal analysis, Data curation, Conceptualization. **Judith Fuentes:** Writing – review & editing, Investigation, Formal analysis. **Carlos Alemán:** Writing – review & editing, Supervision, Conceptualization. **Samuel Sánchez:** Writing – review & editing, Supervision, Project administration, Conceptualization.

Declaration of competing interest

The authors declare the following financial interests/personal relationships which may be considered as potential competing interests: The authors declare no conflict of interest.

BRENDA G. MOLINA reports financial support was provided by Spanish Ministry of Universities. CARLOS ALEMAN reports financial support was provided by Government of Catalonia Agency for Administration of University and Research Grants. CARLOS ALEMAN reports financial support was provided by Government of Catalonia. JUDITH FUENTES reports financial support was provided by European Union. SAMUEL SANCHEZ reports financial support was provided by Government of Catalonia. SAMUEL SANCHEZ reports financial support was provided by Spanish Scientific Research Council. If there are other authors, they declare that they have no known competing financial interests or personal relationships that could have appeared to influence the work reported in this paper.

Data availability

Data will be made available on request.

Acknowledgements

B.G.M is thankful with the Spanish Ministry of Universities for the support through a Margarita Salas postdoctoral grant, founded by European Union – NextGenerationEU. This publication is part of the I+D+i project PID 2021-125767OB-I00 funded by MCIN/AEI/10.13039/501100011033 and, as appropriate, by "ERDF A way of making Europe", by the European Union. Authors are thanked to the *Agència de Gestió d'Ajuts Universitaris i de Recerca* (2021 SGR 00387) for financial support. Support for the research of C.A. was also received through the prize "ICREA Academia" for excellence in research funded by the *Generalitat de Catalunya*. S.S. and J.F. thank the European Union's Horizon Europe research and innovation programme under grant agreement No. 101070328 (Biomeld) and the CERCA program by the Generalitat de Catalunya, *the Secretaria d'Universitats i Recerca del Departament d'Empresa i Coneixement de la Generalitat de Catalunya* through the project 2021 SGR 01606, and the "*Centro de Excelencia Severo Ochoa*", funded by *Agencia Estatal de Investigación* (CEX 2018-000789-S).

Appendix A. Supplementary data

Supplementary data to this article can be found online at https://doi.org/10.1016/j.bios.2024.116117.

References

Abdollahi Baghban, S., Ebrahimi, M., Bagheri-Khoulenjani, S., Khorasani, M., 2021. A highly efficient microwave-assisted synthesis of an LED-curable methacrylated gelatin for bio applications. RSC Adv. 11, 14996–15009. https://doi.org/10.1039/d1ra01269j.

Aggas, J.R., Abasi, S., Phipps, J.F., Podstawczyk, D.A., Guiseppi-Elie, A., 2020. Microfabricated and 3-D printed electroconductive hydrogels of PEDOT:PSS and their application in bioelectronics. Biosens. Bioelectron. 168, 112568 https://doi.org/10.1016/j.bios.2020.112568.

Ahmed, R.E., Tokuyama, T., Anzai, T., Chanthra, N., Uosaki, H., 2022. Sarcomere maturation: function acquisition, molecular mechanism, and interplay with other organelles. Philos. Trans. R. Soc. B Biol. Sci. 377 https://doi.org/10.1098/rstb.2021.0325.

Araya, R., Riquelme, M.A., Brandan, E., Sáez, J.C., 2004. The formation of skeletal muscle myotubes requires functional membrane receptors activated by extracellular ATP. Brain Res. Rev. 47, 174–188. https://doi.org/10.1016/j.brainresrev.2004.06.003.

Asulin, M., Michael, I., Shapira, A., Dvir, T., 2021. One-step 3D printing of heart patches with built-in electronics for performance regulation. Adv. Sci. 8, 1–8. https://doi.org/10.1002/advs.202004205.

Bustamante, M., Fernández-Verdejo, R., Jaimovich, E., Buvinic, S., 2014. Electrical stimulation induces IL-6 in skeletal muscle through extracellular ATP by activating Ca2+ signals and an IL-6 autocrine loop. Am. J. Physiol. Endocrinol. Metab. 306 https://doi.org/10.1152/ajpendo.00450.2013.

Cho, C.H., Woo, J.S., Perez, C.F., Lee, E.H., 2017. A focus on extracellular Ca2+ entry into skeletal muscle. Exp. Mol. Med. 49 https://doi.org/10.1038/emm.2017.208.

Cho, W.W., Kim, B.S., Ahn, M., Ryu, Y.H., Ha, D.H., Kong, J.S., Rhie, J.W., Cho, D.W., 2021. Flexible adipose-vascular tissue assembly using combinational 3D printing for volume-stable soft tissue reconstruction. Adv. Healthcare Mater. 10, 1–12. https://doi.org/10.1002/adhm.202001693.

de Souza, M.F., da Silva, H.N., Rodrigues, J.F.B., Macêdo, M.D.M., de Sousa, W.J.B., Barbosa, R.C., Fook, M.V.L., 2023. Chitosan/gelatin scaffolds loaded with jatropha mollissima extract as potential skin tissue engineering materials. Polymers 15. https://doi.org/10.3390/polym15030603.

Demircan Yalcin, Y., Luttge, R., 2021. Electrical monitoring approaches in 3-dimensional cell culture systems: toward label-free, high spatiotemporal resolution, and high-content data collection in vitro. Organs-on-a-Chip 3, 100006. https://doi.org/10.1016/j.ooc.2021.100006.

Freeman, S., Ramos, R., Alexis Chando, P., Zhou, L., Reeser, K., Jin, S., Soman, P., Ye, K., 2019. A bioink blend for rotary 3D bioprinting tissue engineered small-diameter vascular constructs. Acta Biomater. 95, 152–164. https://doi.org/10.1016/j.actbio.2019.06.052.

Frömter, E., Diamond, J., 1972. Route of passive ion permeation in epithelia. Nat. New Biol. 235, 9–13. https://doi.org/10.1038/newbio235009a0.

Ganji, M., Elthakeb, A.T., Tanaka, A., Gilja, V., Halgren, E., Dayeh, S.A., 2017. Scaling effects on the electrochemical performance of poly(3,4-ethylenedioxythiophene (PEDOT), Au, and Pt for electrocorticography recording. Adv. Funct. Mater. 27, 1703018 https://doi.org/10.1002/adfm.201703018.

Gerasimenko, T., Nikulin, S., Zakharova, G., Poloznikov, A., Petrov, V., Baranova, A., Tonevitsky, A., 2020. Impedance spectroscopy as a tool for monitoring performance in 3D models of epithelial tissues. Front. Bioeng. Biotechnol. 7 https://doi.org/10.3389/fbioe.2019.00474.

Germinario, E., Esposito, A., Midrio, M., Peron, S., Palade, P.T., Betto, R., Danieli-Betto, D., 2008. High-frequency fatigue of skeletal muscle: role of extracellular Ca2+. Eur. J. Appl. Physiol. 104, 445–453. https://doi.org/10.1007/s00421-008-0796-5.

Givan, D.A., 2007. Precious metals in dentistry. Dent. Clin. 51, 591–601. https://doi.org/10.1016/j.cden.2007.03.005.

Guix, M., Mestre, R., Patiño, T., de Corato, M., Fuentes, J., Zarpellon, G., Sánchez, S., 2021. Biohybrid soft robots with self-stimulating skeletons. Sci. Robot. 6, 1–14. https://doi.org/10.1126/SCIROBOTICS.ABE7577.

Guo, J., Asli, A.E.N., Williams, K.R., Lai, P.L., Wang, X., Montazami, R., Hashemi, N.N., 2019. Viability of neural cells on 3D printed graphene bioelectronics. Biosensors 9. https://doi.org/10.3390/bios9040112.

Hanashi, T., Yamazaki, T., Tsugawa, W., Ferri, S., Nakayama, D., Tomiyama, M., Ikebukuro, K., Sode, K., 2009. BioCapacitor-A novel category of biosensor. Biosens. Bioelectron. 24, 1837–1842. https://doi.org/10.1016/j.bios.2008.09.014.

Harris, M.P., 2021. Bioelectric signaling as a unique regulator of development and regeneration. Devenir 148. https://doi.org/10.1242/DEV.180794.

Heid, S., Boccaccini, A.R., 2020. Advancing bioinks for 3D bioprinting using reactive fillers: a review. Acta Biomater. 113, 1–22. https://doi.org/10.1016/j.actbio.2020.06.040.

Kacarevic, Z., Rider, P., Alkildani, S., Retnasingh, S., Smeets, R., Jung, O., Ivanisevic, Z., Barbeck, M., 2018. An introduction to 3D bioprinting: possibilities, challenges and future aspects. Materials 11, 2199. https://doi.org/10.3390/ma11112199.

Kakehi, N., Yamazaki, T., Tsugawa, W., Sode, K., 2007. A novel wireless glucose sensor employing direct electron transfer principle based enzyme fuel cell. Biosens. Bioelectron. 22, 2250–2255. https://doi.org/10.1016/j.bios.2006.11.004.

Kim, D., Shin, M., Choi, J.H., Choi, J.W., 2022. Actuation-augmented biohybrid robot by hyaluronic acid-modified Au nanoparticles in muscle bundles to evaluate drug effects. ACS Sens. 7, 740–747. https://doi.org/10.1021/acssensors.1c02125.

Kong, M., Garriga, M., Reparaz, J.S., Alonso, M.I., 2022. Advanced optical characterization of PEDOT:PSS by combining spectroscopic ellipsometry and Raman scattering. ACS Omega 7, 39429–39436. https://doi.org/10.1021/acsomega.2c05945.

Labazanova, L., Wu, Z., Gu, Z., Navarro-Alarcon, D., 2021. Bio-Inspired design of artificial striated muscles composed of sarcomere-like contraction units, 2021 20th Int. Conf. Adv. Robot.. https://doi.org/10.1109/ICAR53236.2021.9659330. ICAR 2021 370–377.

Lamport, D.T.A., Várnai, P., 2013. Periplasmic arabinogalactan glycoproteins act as a calcium capacitor that regulates plant growth and development. New Phytol. 197, 58–64. https://doi.org/10.1111/nph.12005.

Li, L., Meng, J., Zhang, M., Liu, T., Zhang, C., 2022. Recent advances in conductive polymer hydrogel composites and nanocomposites for flexible electrochemical supercapacitors. Chem. Commun. 58, 185–207. https://doi.org/10.1039/d1cc05526g.

Li, Z., Seo, Y., Aydin, O., Elhebeary, M., Kamm, R.D., Kong, H., Saif, M.T.A., 2019. Biohybrid valveless pump-bot powered by engineered skeletal muscle. Proc. Natl. Acad. Sci. USA 116, 1543–1548. https://doi.org/10.1073/pnas.1817682116.

Ma, Y., Zhang, L., 2022. Formulated food inks for extrusion-based 3D printing of personalized foods: a mini review. Curr. Opin. Food Sci. 44, 100803 https://doi.org/10.1016/j.cofs.2021.12.012.

Manabe, Y., Takagi, M., Nakamura-Yamada, M., Goto-Inoue, N., Taoka, M., Isobe, T., Fujii, N.L., 2014. Redox proteins are constitutively secreted by skeletal muscle. J. Physiol. Sci. 64, 401–409. https://doi.org/10.1007/s12576-014-0334-7.

Mestre, R., García, N., Patiño, T., Guix, M., Fuentes, J., Valerio-Santiago, M., Almiñana, N., Sánchez, S., 2021. 3D-bioengineered model of human skeletal muscle tissue with phenotypic features of aging for drug testing purposes. Biofabrication 13. https://doi.org/10.1088/1758-5090/ac165b.

Molina, B.G., Bendrea, A.D., Lanzalaco, S., Franco, L., Cianga, L., del Valle, L.J., Puiggali, J., Turon, P., Armelin, E., Cianga, I., Aleman, C., 2020. Smart design for a flexible, functionalized and electroresponsive hybrid platform based on poly(3,4-ethylenedioxythiophene) derivatives to improve cell viability. J. Mater. Chem. B 8, 8864–8877. https://doi.org/10.1039/d0tb01259a.

Molina, B.G., Domínguez, E., Armelin, E., Alemán, C., 2018. Assembly of conducting polymer and biohydrogel for the release and real-time monitoring of vitamin K3. Gels 4, 86. https://doi.org/10.3390/gels4040086.

Molina, B.G., Valle, L.J., Casanovas, J., Lanzalaco, S., Pérez-Madrigal, M.M., Turon, P., Armelin, E., Alemán, C., 2021. Plasma-Functionalized isotactic polypropylene assembled with conducting polymers for bacterial quantification by NADH sensing. Adv. Healthcare Mater. 10, 2100425 https://doi.org/10.1002/adhm.202100425.

Oliveira, R., Georgieva, P., Feyo de Azevedo, S., 2002. Plant and equipment | instrumentation and process control: instrumentation. In: Encyclopedia of Dairy Sciences. Elsevier, pp. 234–241. https://doi.org/10.1016/B978-0-12-374407-4.00412-X.

Outrequin, T.C.R., Gamonpilas, C., Siriwatwechakul, W., Sreearunothai, P., 2023. Extrusion-based 3D printing of food biopolymers: a highlight on the important rheological parameters to reach printability. J. Food Eng. 342 https://doi.org/10.1016/j.jfoodeng.2022.111371.

Park, Y.G., Yun, I., Chung, W.G., Park, W., Lee, D.H., Park, J.U., 2022. High-Resolution 3D printing for electronics. Adv. Sci. 9 https://doi.org/10.1002/advs.202104623.

Pérez-Madrigal, M.M., Edo, M.G., Díaz, A., Puiggalí, J., Alemán, C., 2017. Poly-γ-glutamic acid hydrogels as electrolyte for poly(3,4-ethylenedioxythiophene)-based supercapacitors. J. Phys. Chem. C 121, 3182–3193. https://doi.org/10.1021/acs.jpcc.6b10693.

Pillai, S., Upadhyay, A., Khayambashi, P., Farooq, I., Sabri, H., Tarar, M., Lee, K.T., Harb, I., Zhou, S., Wang, Y., Tran, S.D., 2021. Dental 3d-printing: transferring art from the laboratories to the clinics. Polymers 13, 1–25. https://doi.org/10.3390/polym13010157.

Praveena, B.A., Lokesh, N., Buradi, A., Santhosh, N., Praveena, B.L., Vignesh, R., 2022. A comprehensive review of emerging additive manufacturing (3D printing technology): methods, materials, applications, challenges, trends and future potential. Mater. Today Proc. 52, 1309–1313. https://doi.org/10.1016/j.matpr.2021.11.059.

Puiggalí-Jou, A., Micheletti, P., Estrany, F., del Valle, L.J., Alemán, C., 2017. Electrostimulated release of neutral drugs from polythiophene nanoparticles: smart regulation of drug–polymer interactions. Adv. Healthcare Mater. 6, 1–11. https://doi.org/10.1002/adhm.201700453.

Rafienia, M., Imani, R., Hojjati Emami, S., Rabbani, M., Kabiri, M., 2008. Synthesis and characterization of biodegradable hemostat gelatin sponge for surgery application. J. Pharmaceut. Sci. 4, 193–200. Iran.

Rivera, B., Cano, C., Luis, I., Elias, D.A., 2022. A 3D-printed knee wearable goniometer with a mobile-app interface for measuring range of motion and monitoring activities. Sensors 22. https://doi.org/10.3390/s22030763.

Rohde, F., Danz, K., Jung, N., Wagner, S., Windbergs, M., 2022. Electrospun scaffolds as cell culture substrates for the cultivation of an in vitro blood–brain barrier model using human induced pluripotent stem cells. Pharmaceutics 14. https://doi.org/10.3390/pharmaceutics14061308.

Ruano, G., Molina, B.G., Torras, J., Alemán, C., 2021. Free-standing, flexible nanofeatured polymeric films prepared by spin-coating and anodic polymerization as electrodes for supercapacitors. Molecules 26, 1–12. https://doi.org/10.3390/molecules26144345.

Rudge, A., Davey, J., Raistrick, I., Gottesfeld, S., Ferraris, J.P., 1994. Conducting polymers as active materials in electrochemical capacitors. J. Power Sources 47, 89–107. https://doi.org/10.1016/0378-7753(94)80053-7.

Rühl, P., Langner, J.M., Reidel, J., Schönherr, R., Hoshi, T., Heinemann, S.H., 2021. Monitoring of compound resting membrane potentials of cell cultures with ratiometric genetically encoded voltage indicators. Commun. Biol. 4, 1–11. https://doi.org/10.1038/s42003-021-02675-0.

Ruiz, L.E., Pinho, A.C., Resende, D.N., 2022. 3D printing as a disruptive technology for the circular economy of plastic components of end-of-life vehicles: a systematic review. Sustain. Times 14. https://doi.org/10.3390/su142013256.

Ryan, K.R., Down, M.P., Hurst, N.J., Keefe, E.M., Banks, C.E., 2022. Additive manufacturing (3D printing) of electrically conductive polymers and polymer nanocomposites and their applications. eScience 2, 365–381. https://doi.org/10.1016/j.esci.2022.07.003.

Saha, D., Heldt, C.L., Gencoglu, M.F., Vijayaragavan, K.S., Chen, J., Saksule, A., 2016. A study on the cytotoxicity of carbon-based materials. Mater. Sci. Eng. C 68, 101–108. https://doi.org/10.1016/j.msec.2016.05.094.

Shengjie, L., Xiong, Z., Wang, X., Yan, Y., Liu, H., Zhang, R., 2009. Direct fabrication of a hybrid cell/hydrogel construct by a double-nozzle assembling technology. J. Bioact. Compat Polym. 24, 249–265. https://doi.org/10.1177/0883911509104094.

Sordini, L., Garrudo, F.F.F., Rodrigues, C.A.V., Linhardt, R.J., Cabral, J.M.S., Ferreira, F.C., Morgado, J., 2021. Effect of electrical stimulation conditions on neural stem cells differentiation on cross-linked PEDOT:PSS films. Front. Bioeng. Biotechnol. 9, 1–13. https://doi.org/10.3389/fbioe.2021.591838.

Suntornnond, R., An, J., Chua, C.K., 2017. Bioprinting of thermoresponsive hydrogels for next generation tissue engineering: a review. Macromol. Mater. Eng. 302 https://doi.org/10.1002/mame.201600266.

Syuhada, A., Shamsudin, M.S., Omar, M.F., Ghoshal, S.K., Harun, S.W., Aziz, M.S., 2021. Incorporating 3D metal printing with artificial intelligence in meeting aerospace

demands. J. Phys. Conf. Ser. https://doi.org/10.1088/1742-6596/1892/1/012015, 1892.
Tan, H.W., Choong, Y.Y.C., Kuo, C.N., Low, H.Y., Chua, C.K., 2022. 3D printed electronics: processes, materials and future trends. Prog. Mater. Sci. 127, 100945 https://doi.org/10.1016/j.pmatsci.2022.100945.
Thakur, A., Bharti, R., Sharma, R., 2021. Carbon nanotubes: types, synthesis, cytotoxicity and applications in biomedical. Mater. Today Proc. 50, 2256–2268. https://doi.org/10.1016/j.matpr.2021.10.002.
Vijayavenkataraman, S., Yan, W.C., Lu, W.F., Wang, C.H., Fuh, J.Y.H., 2018. 3D bioprinting of tissues and organs for regenerative medicine. Adv. Drug Deliv. Rev. 132, 296–332. https://doi.org/10.1016/j.addr.2018.07.004.
Vu, M., Pramanik, A., Basak, A.K., Prakash, C., Shankar, S., 2022. Progress and challenges on extrusion based three dimensional (3D) printing of biomaterials. Bioprinting 27. https://doi.org/10.1016/j.bprint.2022.e00223.
Wang, J., Dong, S., Ding, B., Wang, Y., Hao, X., Dou, H., Xia, Y., Zhang, X., 2017. Pseudocapacitive materials for electrochemical capacitors: from rational synthesis to capacitance optimization. Natl. Sci. Rev. 4, 71–90. https://doi.org/10.1093/nsr/nww072.
Wang, Y., Wang, Q., Luo, S., Chen, Z., Zheng, X., Kankala, R.K., Chen, A., Wang, S., 2021. 3D bioprinting of conductive hydrogel for enhanced myogenic differentiation. Regen. Biomater. 8, 1–11. https://doi.org/10.1093/rb/rbab035.
Wu, S., Zeng, T., Liu, Z., Ma, G., Xiong, Z., Zuo, L., Zhou, Z., 2022. 3D printing technology for smart clothing: a topic review. Materials 15. https://doi.org/10.3390/ma15207391.
Wu, X., Liu, J., Guo, C., Shi, Z.Z., Zou, Z., Sun, W., Li, C.M., 2022. Living cell-based ultrahigh-supercapacitive behaviours. J. Mater. Chem. A 10, 1241–1247. https://doi.org/10.1039/d1ta09818g.
Xiao, Y.-Q., Kan, C.-W., 2022. Review on development and application of 3D-printing technology in textile and fashion design. Coatings 12, 267. https://doi.org/10.3390/coatings12020267.
Ye, L., Cao, Z., Liu, X., Cui, Z., Li, Z., Liang, Y., Zhu, S., Wu, S., 2022. Noble metal-based nanomaterials as antibacterial agents. J. Alloys Compd. 904, 164091 https://doi.org/10.1016/j.jallcom.2022.164091.
Yi, Q., Najafikhoshnoo, S., Das, P., Noh, S., Hoang, E., Kim, T., Esfandyarpour, R., 2022. All-3D-Printed, flexible, and hybrid wearable bioelectronic tactile sensors using biocompatible nanocomposites for health monitoring. Adv. Mater. Technol. 7, 1–13. https://doi.org/10.1002/admt.202101034.
Yuan, X., Zhang, X., Sun, L., Wei, Y., Wei, X., 2019. Cellular toxicity and immunological effects of carbon-based nanomaterials. Part. Fibre Toxicol. 16 https://doi.org/10.1186/s12989-019-0299-z.
Zhang, S., Liu, Y., Hao, J., Wallace, G.G., Beirne, S., Chen, J., 2022. 3D-Printed wearable electrochemical energy devices. Adv. Funct. Mater. 32 https://doi.org/10.1002/adfm.202103092.
Zheng, M., Wang, X., Yue, O., Hou, M., Zhang, H., Beyer, S., Blocki, A.M., Wang, Q., Gong, G., Liu, X., Guo, J., 2021. Skin-inspired gelatin-based flexible bio-electronic hydrogel for wound healing promotion and motion sensing. Biomaterials 276, 121026. https://doi.org/10.1016/j.biomaterials.2021.121026.
Zhu, Y., Qin, J., Shi, G., Sun, C., Ingram, M., Qian, S., Lu, J., Zhang, S., Zhong, Y.L., 2022. A focus review on 3D printing of wearable energy storage devices. Carbon Energy 4, 1242–1261. https://doi.org/10.1002/cey2.199.